The Pennsylvania State University

The Graduate School

College of Earth and Mineral Sciences

ENERGETICS OF A SINGLE-CELL THUNDERSTORM

A Thesis in

Meteorology

by

Lindsey T. Ritchie

Submitted in Partial Fulfillment
of the Requirements
for the Degree of

Master of Science

December 2008

The thesis of Lindsey T. Ritchie was reviewed and approved* by the following:

Peter R. Bannon
Professor of Meteorology
Thesis Advisor

Paul M. Markowski
Associate Professor of Meteorology

Jerry Y. Harrington
Associate Professor of Meteorology

Eugene E. Clothiaux
Associate Professor of Meteorology
Head of the Graduate Program in Meteorology

*Signatures are on file in the Graduate School

ABSTRACT

A nonlinear moist compressible numerical model is used to simulate deep moist convection generated by a prescribed localized warm bubble. The evolution of the storm is described. Particular attention is focused on two different Eulerian formulations of the storm energetics. The first formulation is the traditional energetics consisting of kinetic, potential, and internal energetics. The second formulation is the available energetics that can be divided into potential, elastic, and chemical energies. Two different thermodynamic schemes are presented, and both schemes are shown to satisfy the thermodynamic constraints on a moist system. The two energy formulations are compared and contrasted for each thermodynamic scheme for two model atmospheres. In the first model atmosphere, all the moisture is in the form of water vapor and no phase changes are allowed. It is shown that this atmosphere produces comparable results to the energetics of a dry atmosphere. In the second model atmosphere, both phase changes and fallout are allowed using the cloud microphysics parameterization of Kessler. With the addition of the enthalpy carried by the precipitation, the total traditional energy is conserved. It is postulated that the total available energy would be conserved with the addition of the available phase change and available rain energies.

TABLE OF CONTENTS

LIST OF FIGURES

LIST OF TABLES

ACKNOWLEDGMENTS

I would like to express my sincere gratitude to my advisor, Dr. Peter R. Bannon, for his support and direction in this research, and for his constructive criticism through the writing process. I am also grateful to my committee members Dr. Paul M. Markowski and Dr. Jerry Y. Harrington. In addition, I would like to thank everyone in 407 Walker and my friends, both here at Penn State and further away, for their help, support, and distractions. Finally, I would like to thank my family for all their love and support, and Stephen for keeping me sane, and for always making me laugh at the end of the day.

The National Science Foundation (NSF) under NSF Grant ATM – 0539969 provided partial support for this research.

Chapter 1
Introduction

The calculation of the convective available potential energy, or CAPE, (e.g., Moncrieff and Miller, 1976; Williams and Renno 1993), which represents the amount of energy available for the vertical convection of a particular parcel of air, is often important in the study of deep moist convection. The formulation of this potential energy was first conceptualized by Margules (1905), but named by Moncrieff and Miller (1976). It is Lagrangian in nature as it focuses on following the vertical movement of a parcel of air and comparing its properties to those of the undisturbed environmental air surrounding it. This procedure is commonly known as parcel theory. For a complete review the reader is referred to Emanuel (1994), Doswell and Markowski (2004), and Holton (2004).

Parcel theory must make an assumption regarding the mass exchange between the parcel and the environment. Therefore, in a moist atmosphere two different assumptions can be made to describe the behavior of moist parcels (e.g., Bohren and Albrecht 1998; Emanuel 2004). In the first assumption, the parcel retains all the liquid water condensed during its moist ascent. Therefore, the heat capacity contribution of the liquid water to the parcel temperature is retained. Subsequent descent of the parcel would occur with moist adiabatic warming, thereby returning the parcel to its original state. Hence, this process is reversible. In the second assumption, all the condensed water is immediately removed from a parcel by idealized instantaneous precipitation. Therefore, in this case, the heat capacity contribution of the liquid water to the parcel temperature is neglected. The latent heat released in the condensation process is retained, however, so this assumption is called pseudoadiabatic. The temperature of a parcel ascending by the reversible process can be as much as 3°C higher than that of a parcel ascending pseudoadiabatically (Bohren and Albrecht, 1998, p. 295). Natural atmospheric parcel ascent lies somewhere in between reversible and pseudoadiabatic ascent.

Another inherent problem with parcel theory is that it neglects the environmental reaction to the parcel displacement (e.g. Emanuel, 1994, p.168). In

addition, Emanuel (1994, p. 183) has also shown that when considering the available potential energy (APE) of the whole system, the actual amount of energy available can be substantially less than that indicated by the parcel CAPE. This result suggests that there is some benefit to studying the Eulerian energetics of the whole system. It is important to note, however, that the formulation of the available energy used by Emanuel (1994) is based on that of Lorenz (1955), in which the reference state is barotropic, hydrostatic and it need not be isothermal. Furthermore, Lorenz (1955) assumes that all atmospheric motions are hydrostatic and thus its relevance to deep convection is questionable. The formulation presented here is that of Bannon (2005), where the reference state is isothermal and hydrostatic, and the atmospheric motions can be nonhydrostatic. This assumption of nonhydrostatic atmospheric motions is more physically realistic as the vertical motion of convection has significant deviations from hydrostatic equilibrium.

The purpose of this paper is to compare and contrast the Eulerian traditional and available energetics of a numerical simulation of a two-dimensional single-cell thunderstorm for two different thermodynamic schemes. Section 2 describes the compressible numerical model, the base state atmosphere, and the initial nonhydrostatic perturbation used. Section 3 describes the evolution of the thunderstorm. Section 4 describes both the traditional and available energetics analyzed in this study. Section 5 describes the thermodynamic constraints on a moist system, and presents two different thermodynamic schemes that satisfy these constraints. Sections 6 and 7 present two case studies of the energetics for both thermodynamic schemes. In section 6 all the water in the atmosphere is in the form of water vapor and no phase changes are allowed. In section 7 the full cloud microphysics parameterization of Kessler is used, and the fallout of liquid water in the form of precipitation is allowed. Section 8 presents the summarized results and conclusions.

Chapter 2
Numerical Model

a. Governing equations

The model atmosphere is a compressible, moist, rotating atmosphere on an *f*-plane. We assume that the moist air consists only of dry air, water vapor, and liquid water, and that the latter can be subdivided into cloud water and rainwater. Furthermore, the water and the surrounding air have the same temperature. The governing model equations in Cartesian coordinates are

$$\frac{D\mathbf{u}}{Dt} = -\frac{1}{\rho_a(1+r)}\nabla p - f\mathbf{k}\times\mathbf{u} - g\mathbf{k} \tag{2.1}$$

$$c_{vm}\frac{DT}{Dt} = -\frac{p}{\rho_a}\nabla\cdot\mathbf{u} - (l_v - R_vT)\frac{Dr_v}{Dt} \tag{2.2}$$

$$\frac{D\rho_a}{Dt} = -\rho_a\nabla\cdot\mathbf{u} \tag{2.3}$$

$$\frac{Dr_v}{Dt} = -\dot{r}_{cond} + \dot{r}_{evap} \tag{2.4}$$

$$\frac{Dr_c}{Dt} = \dot{r}_{cond} - \dot{r}_{auto} - \dot{r}_{coll} \tag{2.5}$$

$$\frac{Dr_r}{Dt} = \dot{r}_{auto} + \dot{r}_{coll} - \dot{r}_{evap} - \dot{r}_{fallout} \tag{2.6}$$

$$p = \rho_a RT(1 + r_v/\varepsilon) \tag{2.7}$$

where the material derivative is defined as

$$\frac{D}{Dt} \equiv \frac{\partial}{\partial t} + (\mathbf{u}\cdot\nabla)\,. \tag{2.8}$$

Here f is the Coriolis parameter, g is the acceleration due to gravity, ∇ is the two-dimensional del operator (in the x and z directions), $\mathbf{k}$ is the unit vector in the z direction, l_v is the latent heat of vaporization and $\varepsilon = R/R_v$. The variables $\mathbf{u}$, ρ_a, p, r_v, r_c, r_r, r and T are the three-dimensional velocity, dry air density, total pressure, water

vapor mixing ratio, cloud water mixing ratio, rainwater mixing ratio, total water mixing ratio and temperature respectively. All flow fields are assumed to be independent of the y direction. The constants c_{vm}, R, and R_v are the specific heat of moist air at constant volume, and the gas constants of dry air and of water vapor. The nondimensional pressure is defined as

$$\pi \equiv \left(\frac{p}{p_{00}} \right)^{R/c_p} \equiv \frac{T}{\theta} \tag{2.9}$$

where $p_{00} = 1000$ hPa and θ is the potential temperature.

b. Numerical techniques

A thorough description of the numerical model is given in Bryan and Fritsch (2002). The model is integrated with third-order Runge-Kutta time differencing and fifth-order spatial derivatives for the advection terms that are written as the sum of a flux form term and a divergence term. This approach improves the conservation of the variable being advected in the model.

The two-dimensional numerical domain is 30 km in height z and 800 km in the horizontal x direction. The grid spacing is 200 m in both the x- and z-directions. A flat, rigid boundary is applied at z = 0 and 30 km where the vertical velocity is set to zero. In the upper 15 km of the domain a Rayleigh damping layer is employed to damp gravity waves (Bryan et. al. 2003). A mirror boundary is applied at the origin, x = 0 km, as the thermodynamic variables and the vertical velocity are symmetric about the origin and the horizontal velocity is asymmetric. At x = 800 km an open boundary condition is applied following Durran and Klemp (1983). Each simulation is forty minutes in duration with a 0.30 s time step.

c. Initial conditions

Initially the model atmosphere is at rest in hydrostatic balance with a surface pressure of 1000 hPa. From the analytic sounding of Weisman and Klemp (1982) the potential temperature, θ, and relative humidity, H_l, profiles are given by

$$\theta(z)=\begin{cases}\theta_0+(\theta_{tr}-\theta_0)\left(\dfrac{z}{z_{tr}}\right)^{5/4}, & z\le z_{tr}\\ \theta_{tr}\exp\left[\dfrac{g}{c_{pa}T_{tr}}(z-z_{tr})\right], & z\ge z_{tr}\end{cases} \tag{2.10}$$

and

$$H_l(z)=\begin{cases}1-0.75\left(\dfrac{z}{z_{tr}}\right)^{5/4}, & z\le z_{tr}\\ 0.25, & z\ge z_{tr}\end{cases}, \tag{2.11}$$

where θ_0 = 300 K is the surface potential temperature, and the tropopause has potential temperature θ_{tr} = 343 K and reference temperature T_{tr} = 213 K at a height of z_{tr} = 12 km. Integrating the hydrostatic relation upwards from the surface, z = 0 km, to the top of the atmosphere, z = 30 km, and using the ideal gas law, (2.10) and (2.11) gives the atmospheric temperature and water vapor mixing ratio profiles. However, near the surface the water vapor mixing ratio r_v is kept constant at a maximum value of 14 g kg^{-1} to approximate a well-mixed boundary layer. These profiles are depicted in Fig. 1. All the physical constants used with their values are listed in Table 1.

The initial warm bubble is generated by a prescribed, two-dimensional diabatic warming of the form

$$\dot{\Theta}=\Delta\theta\cos^2\left(\frac{\pi R}{2}\right)\delta(t) \quad \text{for } R\le 1, \tag{2.12}$$

where $\Delta\theta$ = 4 K is the amplitude of the warming and $\delta(t)$ is the Dirac delta function in time t. Here

$$R=\left[\left(\frac{x-x_o}{x_r}\right)^2+\left(\frac{z-z_o}{z_r}\right)^2\right]^{1/2}, \tag{2.13}$$

where the parameters x_o = 0 and z_o = 3.5 km are the horizontal and vertical locations of the center of the bubble, and x_r = 10 km and z_r = 2.5 km are the horizontal and vertical radii of the diabatic warming (Smith and Bannon, 2008). This perturbation is instantaneously forced at the initial time t = 0.

d. Cloud microphysics

As the ice phase is not being considered in this study, we describe the warm rain processes using the Kessler parameterization. This parameterization is the simplest representation of warm cloud microphysics in widespread use today (e.g. Emanuel, 1994). It assumes that the population of water particles is bimodal, that small cloud drops have a minute terminal velocity compared to typical air velocities, and that raindrops obey the Marshall-Palmer distribution. This parameterization includes terms for the autoconversion, collection, and evaporation (Kessler, 1969). Once the mixing ratio of cloud water reaches the threshold value r_a = 0.001 kg kg^{-1}, cloud water is automatically converted to raindrops at the autoconversion rate k_a = 0.001 s^{-1}, so

$$\dot{r}_{auto} = k_a (r_c - r_a) \geq 0 . \tag{2.14}$$

The rate of collection of cloud droplets by raindrops is given by

$$\dot{r}_{coll} = k_c r_c r_r^{0.875} , \tag{2.15}$$

where k_c = 2.2 s^{-1} is the collection rate and r_r is the rainwater mixing ratio in kg kg^{-1}. Evaporation of rainwater is given by

$$\dot{r}_{evap} = \frac{C_e (1 - r_v / r_{vs})(\rho_a r_r)^{0.525}}{\rho_a (2.03 \times 10^4 + 9.584 \times 10^6 / (r_{vs} p))} , \tag{2.16}$$

where the evaporative ventilation coefficient is

$$C_e = 1.6 + 30.3922 (\rho_a r_r)^{0.2046} . \tag{2.17}$$

Here p is the total pressure of the moist air in Pa, ρ_a is the dry air density in kg m^{-3}, r_v is the water vapor mixing ratio and r_{vs} is the saturation mixing ratio of the water vapor, both given in kg kg^{-1}. Both the evaporation and collection rates are set to zero if negative. The positive definite terminal speed V_t of the falling rainwater in m s^{-1} is

$$V_t = 14.34 (\rho_a r_r)^{0.1346} (\rho_{ref} / \rho_a)^{0.5} , \tag{2.18}$$

in which ρ_{ref} = 1.15 kg m^{-3} is a reference dry air density. The fallout rate of the rainwater is given by

$$\dot{r}_{fallout} = -\frac{1}{\rho_a} \frac{\partial}{\partial z} (\rho_a V_t r_r) . \tag{2.19}$$

It is assumed that the terminal speed of the cloud water is zero.

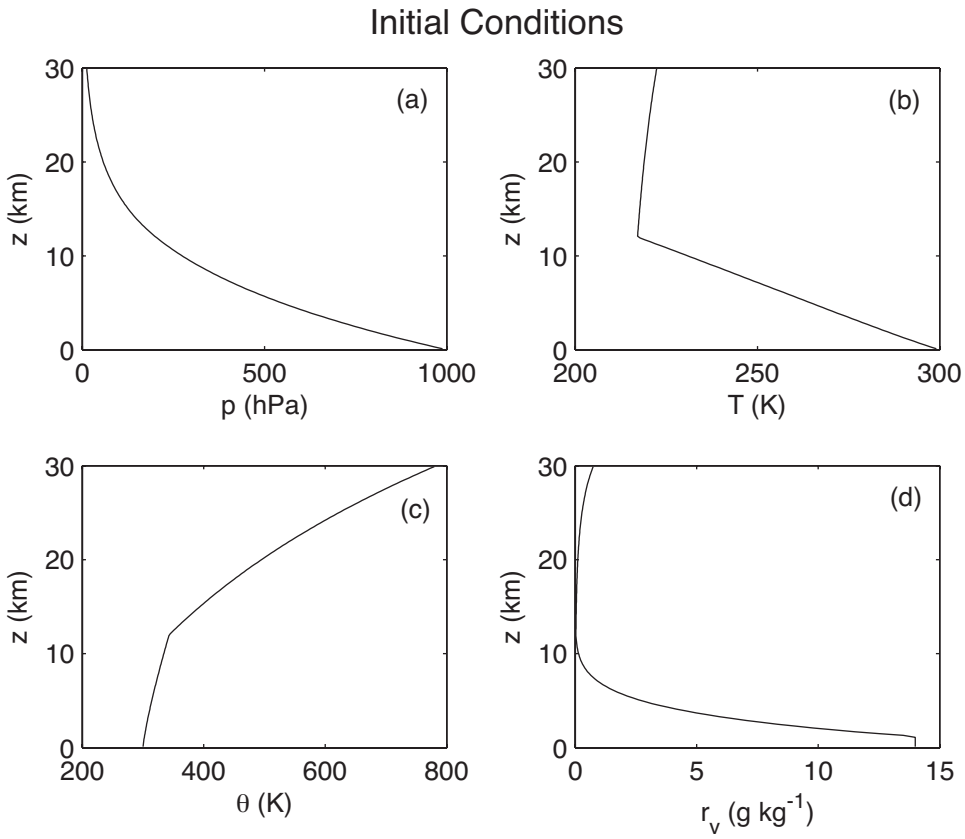

FIG. 1. The (a) pressure, (b) temperature, (c) potential temperature, and (d) water vapor mixing ratio r_v of the base state model atmosphere.

TABLE 1. Physical constants

Parameter	Value
Coriolis parameter	$f = 10^{-4}$ s^{-1}
Acceleration due to gravity	$g = 9.81$ m s^{-1}
Gas constant of dry air	$R = 287$ J kg^{-1} K^{-1}
Gas constant of vapor	$R_v = 461.5$ J kg^{-1} K^{-1}
Ratio of gas constants	$\varepsilon = R/R_v = 0.622$
Specific heat of dry air at constant pressure	$c_p = 1004$ J kg^{-1} K^{-1}
Specific heat of vapor at constant pressure	$c_{pv} = 1885$ J kg^{-1} K^{-1}
Specific heat of liquid water	$c_l = 4218$ J kg^{-1} K^{-1}
Latent heat of vaporization at 0 °C	$l_0 = 2.5003 \times 10^6$ J kg^{-1}
Latent heat of vaporization at 0 K	$l_{00} = 3.14762 \times 10^6$ J kg^{-1}
Reference pressure	$p_{00} = 1000$ hPa
Reference temperature	$T_0 = 273.15$ K

Chapter 3
Temporal Evolution of the Simulated Thunderstorm

This section describes the temporal evolution of the simulated single-cell thunderstorm for the case with phase changes and fallout.

a. Initial conditions

The initial thermodynamic fields are defined as those at time $t = 0$ just before the flow begins and just after the diabatic warming. At this time the three-dimensional wind perturbations *u'*, *v'*, and *w'* are zero, so all perturbations in the initial conditions are as a result of the instantaneous diabatic warming defined in Section 2b.

The perturbation flow field initial conditions are presented in Figure 2. Here perturbation is defined as the departure from the base state value before warming given by the analytic sounding of Weisman and Klemp (1982) described in Section 2b. The instantaneous diabatic warming (2.12) has a potential temperature perturbation of 4 K (Fig. 2a), a pressure perturbation (Fig. 2b), and a temperature perturbation (Fig 2c.). As there is no motion in the model domain, there is no advection of mass, and therefore no density perturbation (Fig. 2d). All the perturbations are confined to the region of the warming, $x \le 10$ km and $1 \le z \le 6$ km. Initially the moisture fields only consists of water vapor as detailed in Section 2b and Figure 1d and thus the moisture perturbations are identically zero.

b. Temporal evolution at 1 minute

The flow perturbations within 30 km of the origin after one minute are shown in Figure 3. A dipole pressure perturbation has developed below 10 km and within 15 km of the origin (Fig. 3a). This dipole has a maximum pressure perturbation of over 50 Pa, and a minimum of -170 Pa. There is also the formation of an updraft near the origin and a downdraft around $x = 9$ km with outflow aloft and inflow at the surface (Fig. 3c and e). These together produce divergence and cause the negative density perturbation (Fig. 3b).

Beyond x = 15 km we can see evidence in the p' and u' fields of a Lamb wave packet propagating horizontally from the origin, centered at x = 22 km. This packet contains the largest pressure perturbation of over 160 Pa (Fig. 3a), with outflow (Fig. 3c). Above 10 km there is also evidence of the vertically propagating acoustic modes near the origin in the pressure, vertical velocity, and temperature fields.

Figure 4 presents the moisture fields within 30 km of the origin after one minute. The water vapor mixing ratio (Fig. 4a) is uniformly distributed in the horizontal direction, with a maximum of 14 g kg^{-1} near the surface. The updraft/downdraft couplet seen near the origin (Fig. 3e) has resulted in the formation of a horizontal dipole water vapor perturbation (Fig. 4b) and the cloud base can clearly be seen at a height of about 1 km. As the vapor pressure has yet to reach saturation vapor pressure there is no cloud water, and subsequently no rainwater has formed (Fig. 4c and d).

c. Temporal evolution at 10 minutes

Figure 5 presents the flow perturbations within 40 km of the origin. The tropopause around 12 km is particularly apparent in the temperature and potential temperature fields with the distortion in the negative perturbation at z = 12 km (Fig. 5d and f). Comparing panels a and c it is seen that there is a strong correlation between the positive pressure perturbation and flow in the positive x-direction above 5 km, and with the negative pressure perturbation and flow in the negative x-direction below 5 km.

Beyond about 100 km from the origin there are additional perturbations in all fields due to the Lamb wave packet (Fig. 6). The double maximum pressure perturbation has propagated about 200 km from the diabatic origin, suggesting a speed of around 333 m s^{-1}. The maximum pressure (Fig. 6a) and density (Fig. 6b) perturbations are at the surface, whereas the maximum horizontal wind perturbation (Fig. 6c) is aloft. The vertical velocity is nonzero (Fig. 6e) because the base state is nonisothermal. This upward motion produces a weak negative potential temperature perturbation. These results agree with those of Smith and Bannon (2008), which suggests that the Lamb wave packet is driven by the initial diabatic warming, and not by the condensation process.

Figure 7 presents the moisture fields after ten minutes. The water vapor mixing ratio is starting to deviate from its horizontal structure near the origin (Fig. 7a), and the vapor perturbation dipole has increased in magnitude (Fig. 7b). The vapor pressure has now reached saturation vapor pressure and so cloud water has been formed near the origin (Fig. 7c). The cloud water mixing ratio has exceeded the autoconversion threshold value of 0.001 kg kg^{-1}, therefore some of this cloud water has been converted to rainwater (Fig. 7d). In panels b, c, and d a clearly defined cloud base can be seen.

At this time the simulated thunderstorm has many features that correlate with the cumulus stage of thunderstorm development described by Byers and Braham (1948). An updraft of 6 m s^{-1} centered at the origin (Fig. 5e) extends throughout the entire cloud (Fig. 7c), and is balanced by a gentle downdraft of almost 2 m s^{-1} just outside of the cloud at x = 4 km. Furthermore, in Figure 5c there is evidence of horizontal convergence at the surface and divergence centered at the cloud top (z = 6 km). Within the cloud, the temperature is almost 3 K higher than in the environment as a result of the condensational warming occurring in the updraft.

d. Evolution of the moisture fields at 20 minutes

Figure 8 presents the moisture fields after twenty minutes. The water vapor mixing ratio has now deviated even further from its initial horizontal structure near the origin (Fig. 8a), and the vapor perturbation dipole (Fig. 8b) has further increased in magnitude, with the negative perturbation stretching further in the x direction, and the positive perturbation stretching further in the z direction. In panels b, c, and d the cloud structure can clearly be seen, with a cloud top close to the tropopause at z = 12 km, and a cloud base at z = 2 km. Both the cloud water and rainwater mixing ratios have increased (Fig. 8c and d), and rainwater has begun to fall to the ground as precipitation. In the region of precipitation (Fig. 8d), a slight positive water vapor perturbation can be seen (Fig. 8b). This vapor perturbation suggests that some of the rainwater is evaporating as it falls into the subsaturated region below the cloud base.

Again, correlations can be made at this time between the simulation and the mature stage of thunderstorm development described by Byers and Braham (1948). This stage is marked by the beginning of precipitation and the formation of a downdraft

in the previous location of the updraft, as can be seen in Figure 9a at t = 20 minutes. Furthermore, this stage is also marked by horizontal divergence at the surface and at cloud top, and horizontal convergence in the mid layer (not shown).

e. Vertical velocity at center of the diabatic warming and evolution of moisture fields

Figure 9 presents the time evolution of the vertical velocity, cloud water mixing ratio, and the rainwater mixing ratio. From panel a it is seen that the first half of the simulation ($t \leq 20$ minutes) is dominated by updrafts, whereas the second half is dominated by downdrafts. In addition, the warm bubble rising forms an updraft (Fig. 9a) which cools and condenses the water vapor to form cloud water with zero terminal velocity (Fig. 9b). Once the cloud water reaches the threshold value of 0.001 kg kg^{-1}, a fraction of the cloud water is automatically converted to rainwater with a nonzero terminal velocity. This rainwater first reaches the surface around 19 minutes (Fig. 9c), which can be correlated with the beginning of a downdraft (Fig. 9a). The precipitation continues to the end of the simulation, along with downdrafts to the surface. The domination of downdrafts and the loss of cloud water after about 23 minutes suggest that the storm is now in its dissipation stage (Byers and Braham, 1948).

For our base state sounding (detailed in Section 2b) with a surface mixing ratio of 14 g kg^{-1}, Weisman and Klemp (1984) calculate the CAPE to be ~2200 m^2 s^{-2} based on the moist adiabatic ascent of a parcel from near the surface. This CAPE value can be used to give an upper bound on the maximum vertical velocity w as

$$w = \sqrt{2CAPE}\,. \tag{3.1}$$

Here, our CAPE value corresponds to a maximum vertical velocity of ~66.3 m s^{-1}. The maximum vertical velocity of the simulation, however, was 39.6 m s^{-1}. Therefore, CAPE grossly overestimates the upper bound on the vertical velocity.

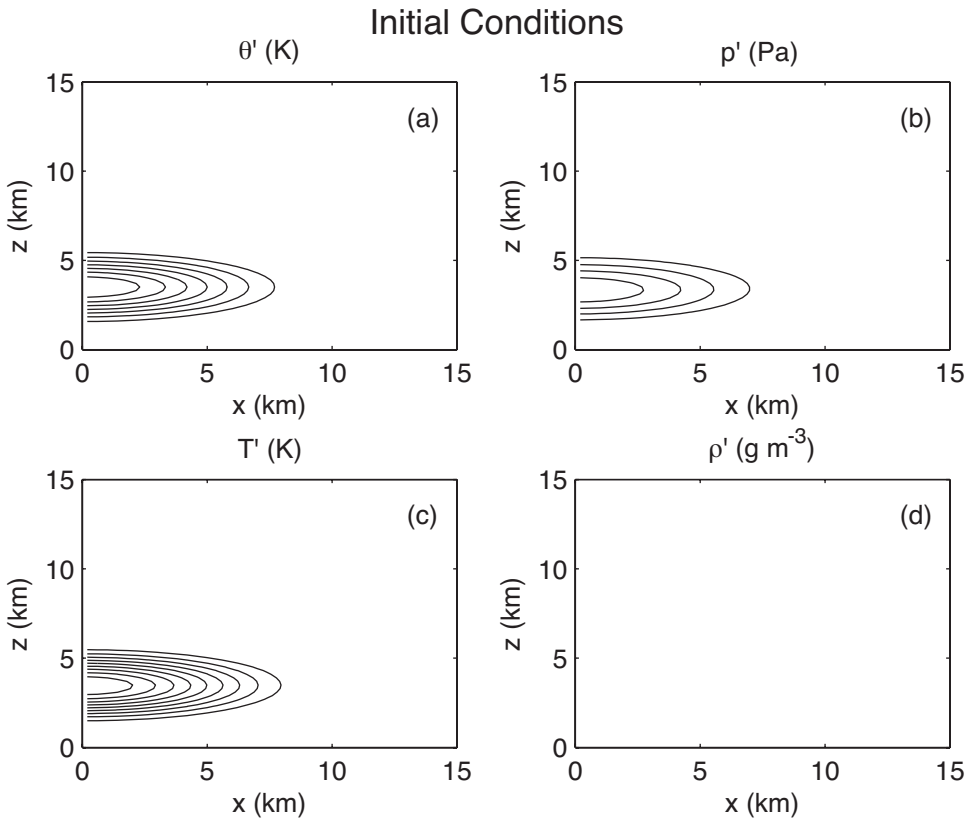

FIG. 2. The initial (a) potential temperature perturbation, (b) pressure perturbation, (c) temperature perturbation, and (d) density perturbation. The contour interval in (a) and (c) is 0.5 K, in (b) is 250 Pa, and in (d) is 0.5 g m^{-3}. Here and elsewhere the solid contours denote positive values and the zero contours are omitted.

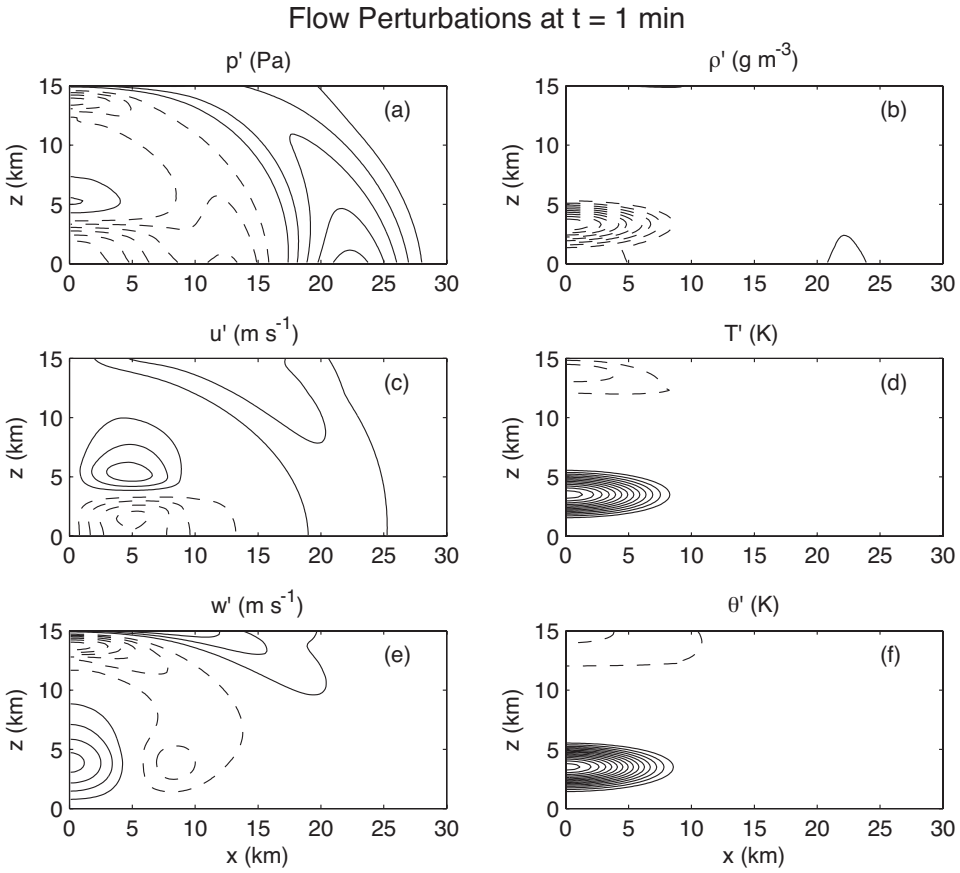

FIG. 3. Perturbations at time t = 1 minute of (a) pressure with a contour interval of 25 Pa, (b) density with an interval of 1 g m^{-3}, (c) horizontal velocity in the x-direction with an interval of 0.25 m s^{-1}, (d) temperature with an interval of 0.25 K, (e) vertical velocity with an interval of 0.25 m s^{-1}, and (f) potential temperature with an interval of 0.25 K. Here and elsewhere dashed contours denote negative values.

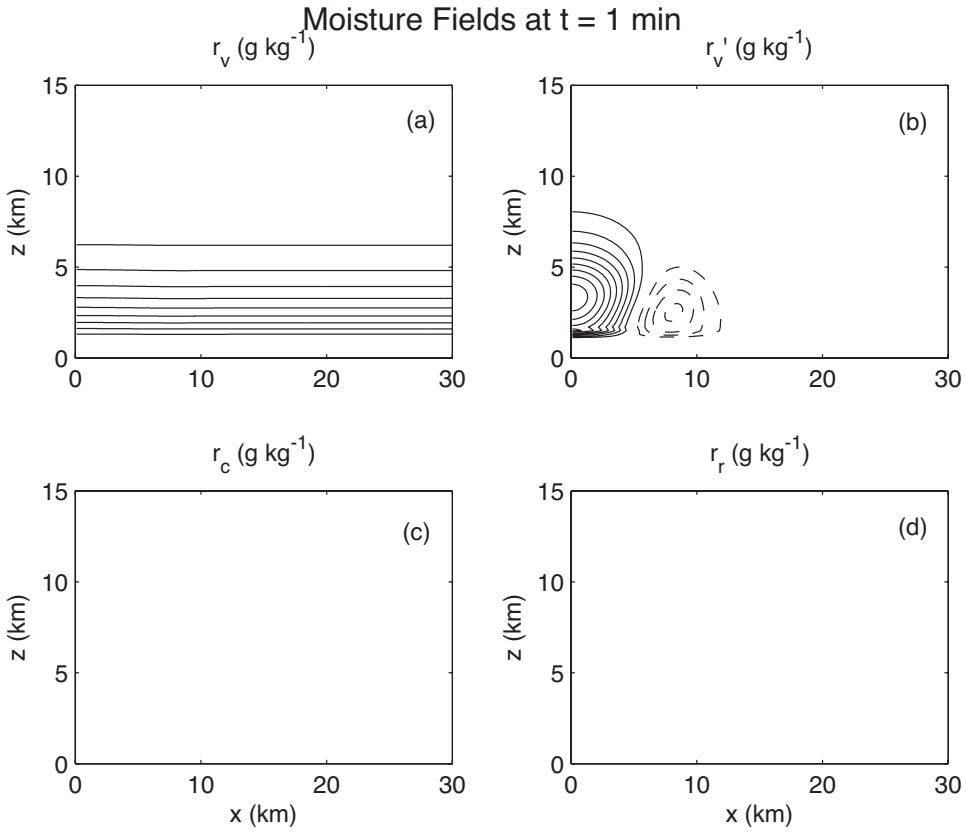

FIG. 4. Moisture fields at time t = 1 minute. Here (a) is the water vapor mixing ratio with interval of 1.5 g kg^{-1}, (b) is the water vapor mixing ratio perturbation with interval of 0.01 g kg^{-1}, (c) is the cloud water mixing ratio, and (d) is the rainwater mixing ratio.

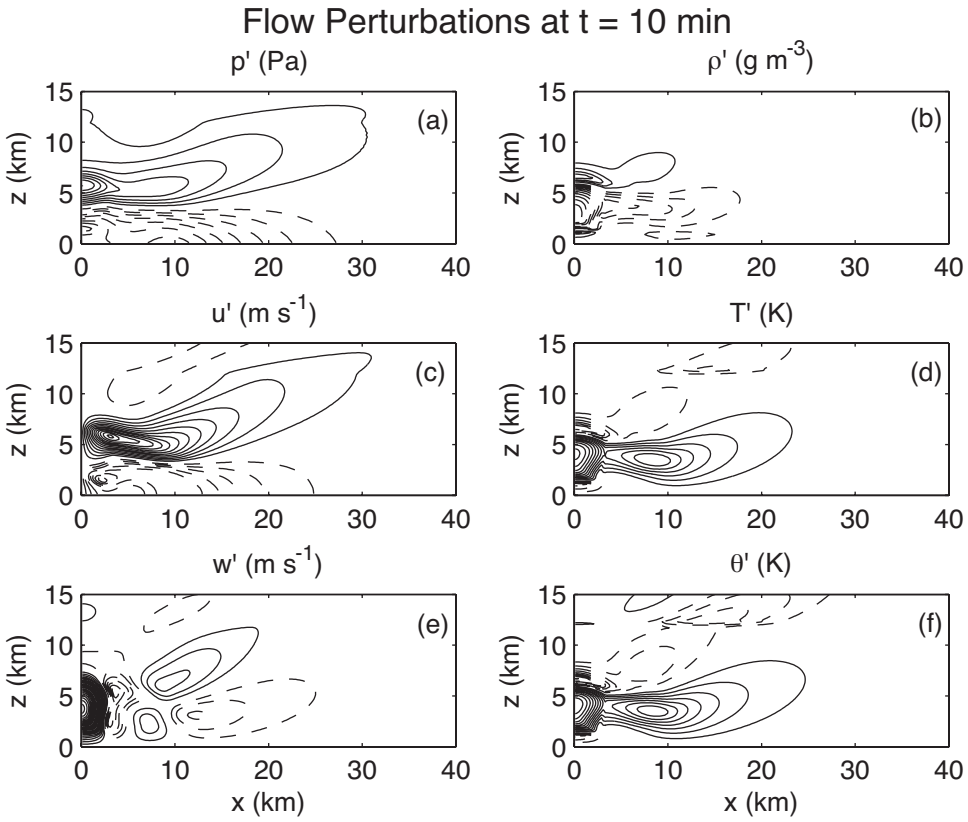

FIG. 5. As in Fig. 3 but for the perturbations at time t = 10 minutes. Intervals are (a) 10 Pa, (b) 1 g m^{-3}, (c) 0.5 m s^{-1}, (d) 0.25 K, (e) 0.25 m s^{-1}, and (f) 0.25 K.

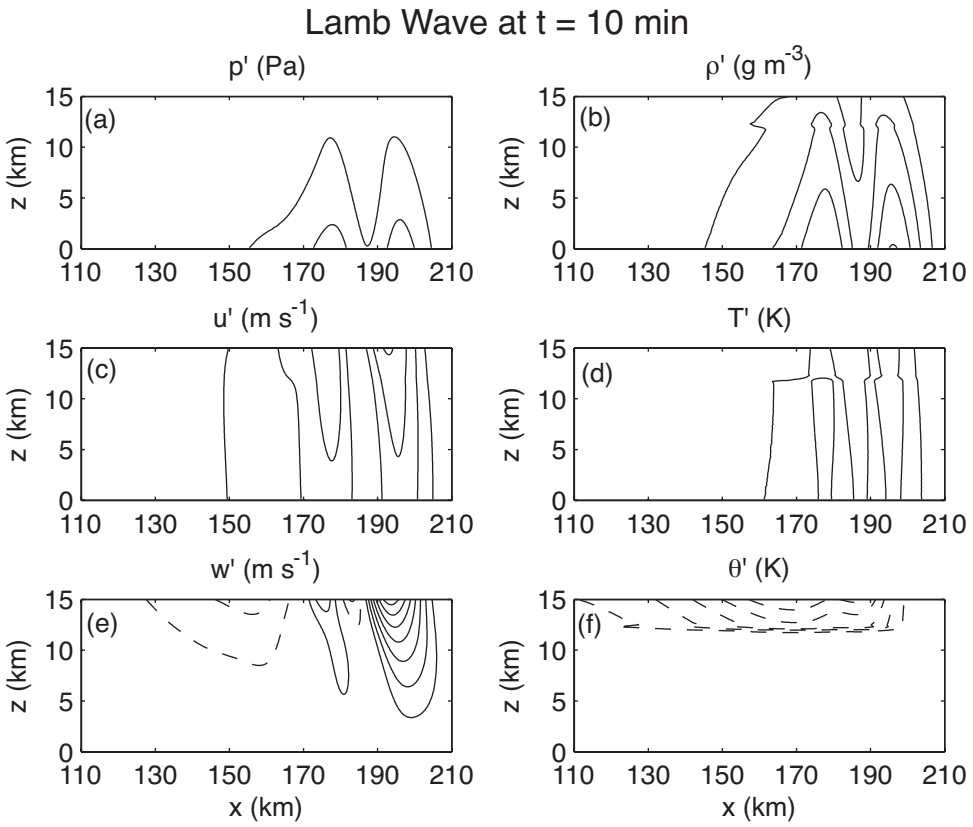

FIG. 6. Lamb wave perturbations at t = 10 minutes of (a) pressure with a contour interval of 10 Pa, (b) density with an interval of 0.05 g m^{-3}, (c) horizontal velocity in the x-direction with an interval of 0.025 m s^{-1}, (d) temperature with an interval of 0.01 K, (e) vertical velocity with an interval of 0.005 m s^{-1}, and (f) potential temperature with an interval of 0.005 K.

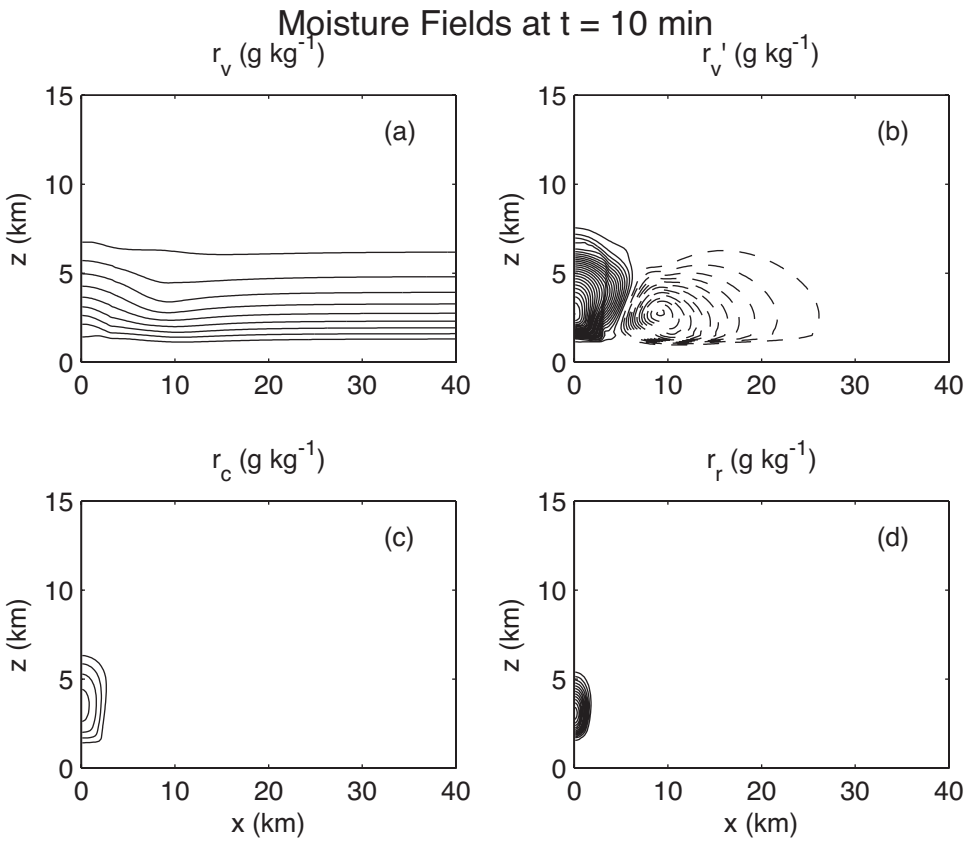

FIG. 7. As in Fig. 4 but for t = 10 minutes. Intervals are (a) 1.5 g kg^{-1}, (b) 0.1 g kg^{-1}, (c) 0.5 g kg^{-1}, and (d) 1.5 x 10^{-5} g kg^{-1}.

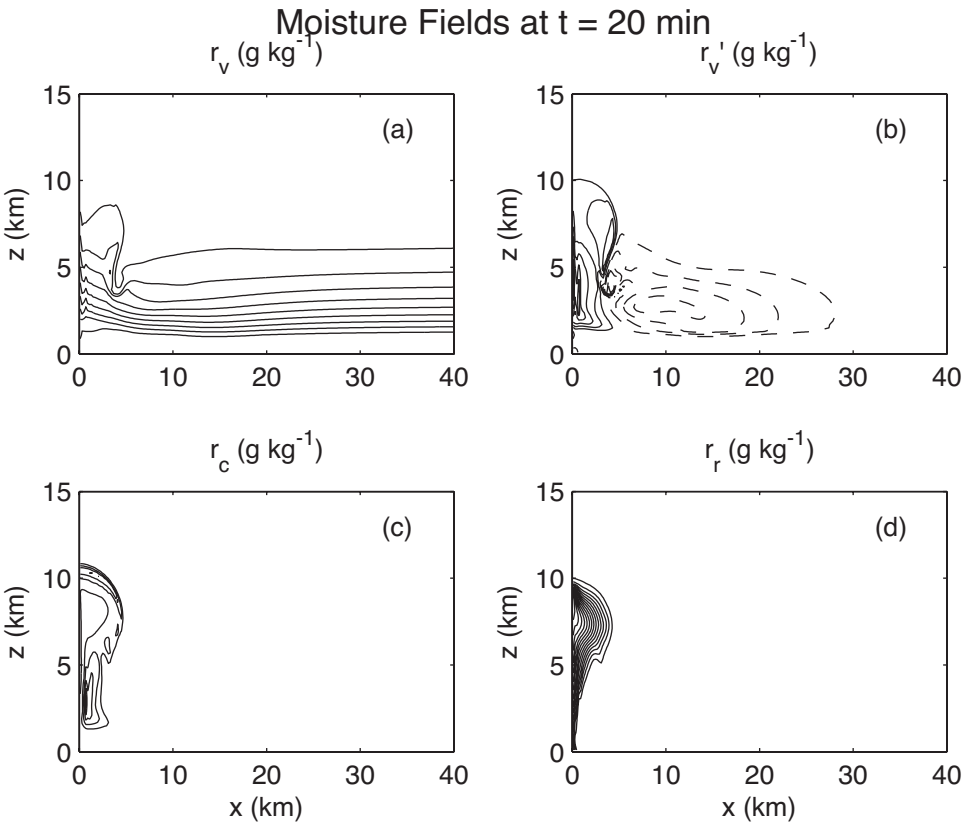

FIG. 8. As in Fig. 4 but for t = 20 minutes. Intervals are (a) 1.5 g kg^{-1}, (b) 0.5 g kg^{-1}, (c) 0.5 g kg^{-1}, and (d) 0.001 g kg^{-1}.

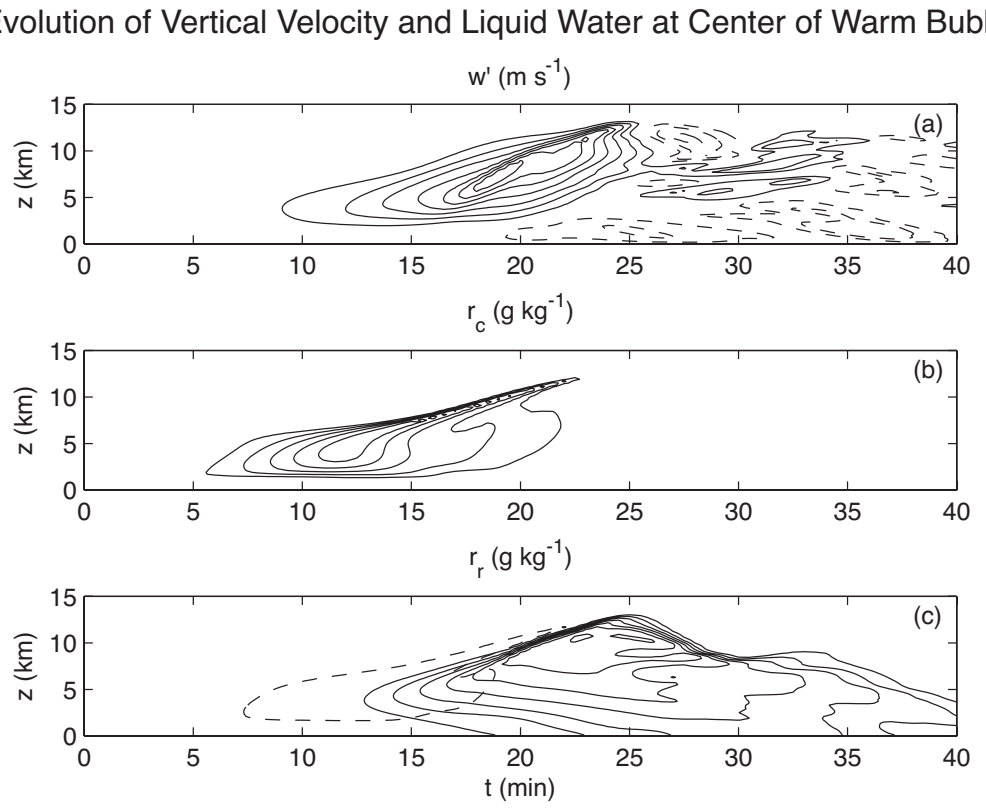

FIG. 9. The evolution of the (a) vertical velocity with contour interval 5 m s^{-1}, (b) the cloud water mixing ratio with interval 0.5 g kg^{-1}, and (c) the rainwater mixing ratio with interval 2.5 g kg^{-1}. The dashed contour in (c) is the second contour of the cloud water mixing ratio in (b).

Chapter 4
Energetics

This section describes the traditional and Eulerian available energetics that will be compared for each thermodynamic scheme presented in Section 5. Traditional energetics includes potential (PE) and internal energies (IE). The available energetics includes available potential (APE), available elastic (AEE), and available chemical energies (ACE). Kinetic energy (KE) is present in both energy types.

a. Traditional energetics

The traditional total energy *TE* is given by

$$TE = KE + PE + IE \tag{4.1}$$

where

$$KE = \int\int \frac{1}{2}\rho_{tot}(u^2 + v^2 + w^2)\, dx\, dz\,, \tag{4.2}$$

$$PE = \int\int \rho_{tot} gz\, dx\, dz\,, \tag{4.3}$$

and,

$$IE = \int\int \rho_{tot}\left(h - \frac{p}{\rho_{tot}}\right) dx\, dz\,, \tag{4.4}$$

in which the specific enthalpy *h* is defined as

$$(1+r)h \equiv h_a + r_v h_v + r_l h_l\,. \tag{4.5}$$

Here ρ_{tot} is the total air density, $r = r_v + r_l$ is the total water mixing ratio, and the subscripts *a*, *v*, and *l* represent the dry air, water vapor, and liquid water respectively. The integrals are taken over the model domain. In (4.2) we have ignored the contribution of the fall speed energy of the rainwater.

b. Eulerian available energetics

The Eulerian available energy, *ae*, (e.g., Bannon 2005) is defined as the difference in the Gibbs function of the atmosphere and a reference state

$$ae = \Delta h - T_{ref}\Delta s - \alpha\Delta p - \mu_{ref,j}\Delta\chi_j\,. \tag{4.6}$$

Here Δ represents a finite departure from the reference state denoted with the subscript *ref* (e.g., $\Delta p = p - p_{ref}$). The four terms on the right-hand side represent the departure in specific enthalpy h given by (4.5), the departure in specific entropy s defined as $(1+r)s \equiv s_a + r_v s_v + r_l s_l$, the departure in pressure p and the departure in concentration χ of the *j*th constituent, respectively. Here $\alpha = 1/\rho$ is the specific volume and T_{ref} and p_{ref} are the temperature and pressure of a reference atmosphere in hydrostatic balance that is assumed to be isothermal with constant concentrations, $\chi_{ref,j}$, and constant chemical potential, $\mu_{ref,j}$. The summation convention holds for repeated subscripts j.

The form of (4.6) allows the partitioning of the available energy into available potential, available elastic and available chemical contributions, such that

$$ae = ape + aee + ace. \tag{4.7}$$

The Eulerian available potential energy

$$ape = h(s, p_{ref}, r) - h(s_{ref}, p_{ref}, r) - T_{ref}\Delta s \tag{4.8}$$

represents the energy associated with the departure of the flow's entropy from the reference entropy. Here enthalpy is a function of entropy, pressure and the total water mixing ratio *r*. The Eulerian available elastic energy

$$aee = h(s, p, r) - h(s, p_{ref}, r) - \alpha\Delta p \tag{4.9}$$

represents the energy associated with the departure of the flow's pressure from the reference pressure. The Eulerian available chemical energy is given by

$$ace = h(s_{ref}, p_{ref}, r) - h(s_{ref}, p_{ref}, 0) - \mu_{ref,j}\Delta\chi_j \tag{4.10}$$

and represents the energy associated with the departure of the chemical concentration of the *j*th component from its reference concentration.

c. Rain energy

The model atmosphere is an open system as water can leave the domain as precipitation. When the precipitation leaves the domain, each drop carries with it a certain amount of energy in the form of an enthalpy. This enthalpy of precipitation is defined as the portion of the total enthalpy that is found in the liquid water at the

surface, that is, the precipitation that has reached the lower boundary of the model, and it has a different form for each thermodynamic scheme discussed in Section 5.

The total enthalpy defined by (4.5), can be repartitioned as

$$(1+r)h = h_a + rh_v - r_l l_v \tag{4.11}$$

using the thermodynamic constraint $h_v - h_l = l_v$ (detailed in Section 5). Rearranging gives

$$(1+r)h = h_a + r_v h_v + r_l (h_v - l_v) \tag{4.12}$$

and therefore the enthalpy carried by the precipitation, or the rain energy, is given by

$$E_{rain} = \sum m_{rain} (h_v - l_v) \tag{4.13}$$

where m_{rain} is the mass per unit length in y of rain at the lower boundary, and the summation is taken over all the grid points on the lower boundary of the model domain. Substituting the differing specific enthalpies of water vapor from each thermodynamic scheme detailed in Section 5 gives two different formulations of the rain energy.

Chapter 5
Moist Thermodynamics

This section describes the two thermodynamic schemes that are used to calculate the traditional and available energetics of the single-cell thunderstorm. Both of these schemes are based on traditional thermodynamics (e.g. Emanuel (1994)).

In both schemes the total specific enthalpy *h,* and the total specific entropy *s* are defined as

$$(1+r)h \equiv h_a + r_v h_v + r_l h_l , \tag{5.1}$$

and

$$(1+r)s \equiv s_a + r_v s_v + r_l s_l . \tag{5.2}$$

Here, $r = r_v + r_l$ is the total water mixing ratio and the subscripts *a*, *v*, and *l* represent the dry air, water vapor, and liquid water respectively.

The enthalpies and entropies of both thermodynamic schemes satisfy the following four thermodynamic constraints on a moist system. The latent heat of vaporization l_v has to satisfy Kirchhoff's equation

$$\frac{dl_v}{dT} = c_{pv} - c_l , \tag{5.3}$$

where c_{pv} is the specific heat of water vapor at constant pressure, and c_l is the specific heat of liquid water. The equilibrium vapor pressure *e** must satisfy the Clausius-Clapeyron equation

$$\frac{de*}{dT} = \frac{l_v e*}{R_v T^2} . \tag{5.4}$$

Here R_v is the gas constant of water vapor. The enthalpies of the water vapor and liquid water are constrained by the phase change process and must satisfy

$$h_v - h_l = l_v , \tag{5.5}$$

where l_v is the latent heat of vaporization. Lastly, the entropy of vapor at the equilibrium vapor pressure s_v^* and the entropy of the liquid water s_l has to satisfy

$$s_v^* - s_l = \frac{l_v}{T} . \tag{5.6}$$

Both of the thermodynamic schemes detailed below satisfy the constraints (5.3) - (5.6).

a. Bannon thermodynamic scheme

This thermodynamic scheme is detailed in Bannon (2005). Here the latent heat of vaporization is given by

$$l_v = l_0 + (c_{pv} - c_l)(T - T_{tp}) \tag{5.7}$$

where l_0 = 2.5003 x 10^6 J kg^{-1} is the reference value of the latent heat of vaporization at T = 0 °C = 273.15 K, and T_{tp} = 275.16 K is the triple point of water. The enthalpies of dry air and water vapor are defined as

$$h_a = h_{a0} + c_p(T - T_0)\,, \tag{5.8}$$

and

$$h_v = h_{v0} + c_{pv}(T - T_0) \tag{5.9}$$

where h_{a0} = 2.735 x 10^5 J kg^{-1} is the reference enthalpy for dry air, and h_{v0} = 5.031 x 10^5 J kg^{-1} is the reference enthalpy for water vapor. The entropies of dry air and water vapor are defined as

$$s_a = s_{a0} + c_p \ln\frac{T}{T_0} - R \ln\frac{p_a}{p_{00}}, \tag{5.10}$$

and

$$s_v = s_{v0} + c_{pv} \ln\frac{T}{T_0} - R_v \ln\frac{e}{e_0^*} \tag{5.11}$$

where s_{a0} = 6.612 x 10^3 J kg^{-1} K^{-1} is the reference entropy for dry air, and s_{v0} = 1.032 x 10^4 J kg^{-1} K^{-1} is the reference entropy for water vapor. Also, e is the vapor pressure, and e_0^* is the reference saturation vapor pressure. The specific enthalpy and entropy for liquid water are not explicitly defined. Instead they are derived from the thermodynamic constraints (5.5) and (5.6).

b. Satoh thermodynamic scheme

This thermodynamic scheme is detailed in Satoh (2003). It defines the latent heat of vaporization as

$$l_v = l_{00} + (c_{pv} - c_l)T\,. \tag{5.12}$$

Here $l_{00} = l_0 - (c_{pv} - c_l)T_0$ is the latent heat defined at 0 K. The only difference between this formulation of the latent heat of vaporization and that given by the Bannon scheme in (5.7) is the choice of reference temperature. The enthalpies of dry air, water vapor, and liquid water are defined as

$$h_a = c_p T \,, \tag{5.13}$$

$$h_v = c_{pv} T + l_{00} \,, \tag{5.14}$$

and

$$h_l = c_l T \,. \tag{5.15}$$

The entropies of dry air, water vapor, and liquid water are defined as

$$s_a = c_p \ln \frac{T}{T_0} - R \ln \frac{p_a}{p_{00}} \,, \tag{5.16}$$

$$s_v = c_{pv} \ln \frac{T}{T_0} - R \ln \frac{e}{e_0^*} + \frac{l_0}{T_0} \,, \tag{5.17}$$

and

$$s_l = c_l \ln \frac{T}{T_0} \,. \tag{5.18}$$

Unlike the thermodynamic scheme of Bannon, this scheme does not include any reference values for the specific enthalpy and entropy of dry air and water vapor. It does, however, add constants to the specific enthalpy and entropy of water vapor, but these constants are not equal to the reference values used in the Bannon scheme.

Chapter 6
Simulation with No Phase Change

This section compares the traditional and available energetics of both thermodynamic schemes for the simulation with no phase changes. The model atmosphere is as described in Section 2b. The saturation vapor mixing ratio r_{vs} is set sufficiently high so that the vapor mixing ratio r_v never reaches this value, and therefore the vapor never condenses to form cloud water. Under each scheme, both the total traditional and total available energies are approximately conserved.

a. Traditional energetics

Even with different formulations of the enthalpy, and therefore different formulations of the internal energy, both thermodynamic schemes have very similar traditional energetic perturbations (Figures 10a and 11a). These can be compared to the compressible traditional energy perturbation in a dry atmosphere (Smith and Bannon, 2008). Initially the kinetic energy of the flow is zero, and the energy generated by the diabatic warming is contained in the internal energy. This internal energy is mainly converted into potential energy as the warm bubble ascends, with a small increase in the kinetic energy. There is a damped oscillation in both the internal and potential energy fields with a period of about 2 minutes, and initial amplitude of about 15 x 10^9 J m^{-1}. These oscillations are 180° out of phase, however. Rising motion results in adiabatic cooling, which decreases the internal energy, and an increase in the mass aloft, which increases the potential energy. The opposite holds for sinking motion. The total energy also decreases slightly in the first few minutes because of the dissipation of the vertically propagating acoustic modes. Both of these phenomena are attributed to the Rayleigh damping layer in the stratosphere (Smith and Bannon, 2008). The kinetic energy increases gradually from an initial value of zero to a final value of 0.21 x 10^9 J m^{-1} through the simulation for both thermodynamic schemes. In addition, for both schemes the total energy decreases approximately 2.0 x 10^9 J m^{-1} through the simulation.

b. Available energetics

As with the traditional energetics, even with different formulations of the enthalpy and entropy, both schemes have similar available energy perturbations (Figure 10b and 11b). Again these are both similar to the dry available energetics of Smith and Bannon (2008), but with the addition of the available chemical energy.

Figure 10b presents the temporal evolution of the available energetics for the Bannon thermodynamic scheme. Initially the energy of the diabatic warming is contained in both the available elastic and potential energies. These exhibit a damped oscillation with initial amplitude of about 1 x 10^9 J m^{-1}. This oscillation is analogous to, but weaker than, that in the traditional energetics (Fig. 10a).

The available energetics of the Satoh thermodynamic scheme is presented in Figure 11b. Initially the energy of the diabatic warming creates a slight negative perturbation in the available elastic energy and a positive perturbation in the available potential energy. Again, both of these energies exhibit a damped oscillation analogous to, but weaker than, that in the traditional energetics (Fig. 11a). Under the Satoh scheme the initial oscillation has a slightly larger amplitude than under the Bannon scheme.

With both schemes there is a net decrease of approximately 2 x 10^9 J m^{-1} in the available potential energy as the available elastic, available chemical and kinetic energies increase in the first ten minutes. The available chemical increases to a value of 0.4 x 10^9 J m^{-1} under both schemes, which is double the contribution from the kinetic energy. The total energy decreases only 0.29 x 10^9 J m^{-1} over the forty minute simulation (Table 2).

c. Lamb wave

Approximate conservation of total traditional and available energies is possible because the Lamb wave packet does not leave the model domain through the forty minute simulation. If the Lamb wave packet propagates out of the domain, it carries with it most of the traditional internal and potential energy as well as most of the available potential energy (not shown, but see Smith and Bannon (2008) for an example).

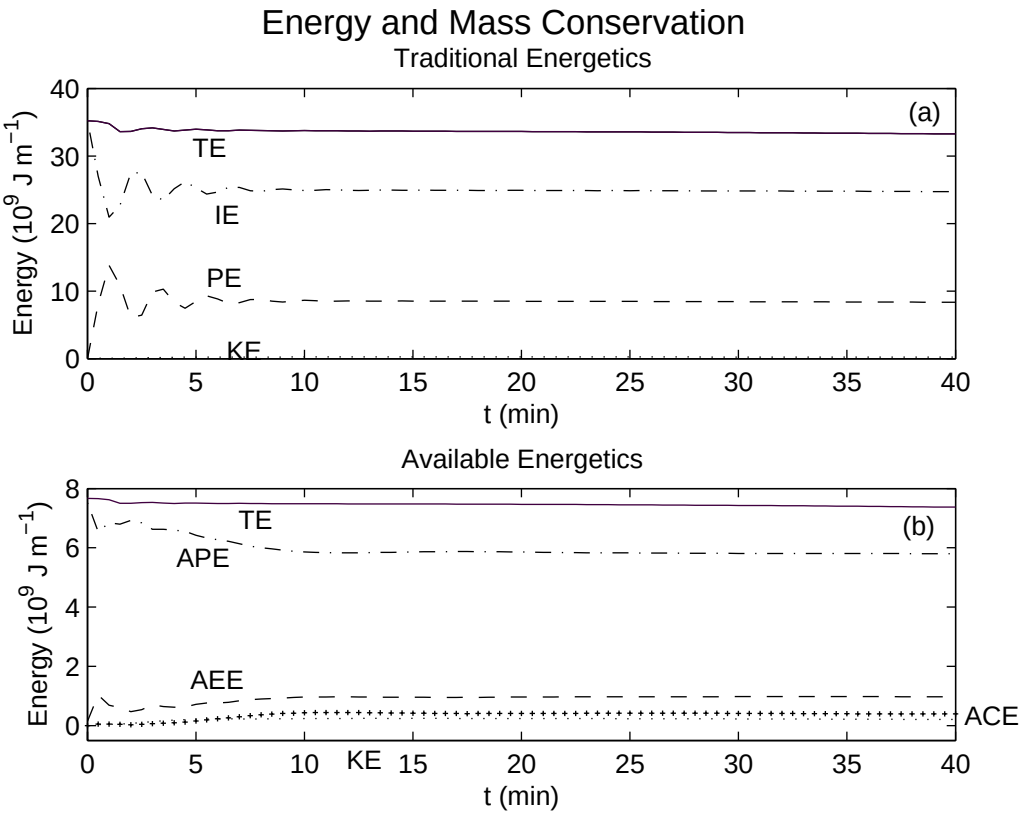

FIG. 10. Domain integrals of the perturbation (a) traditional and (b) available energy in 10^9 J m^{-1} as functions of time for the Bannon thermodynamic scheme. In (a) the curves for internal energy (IE) and potential energy (PE) are dashed-dotted and dashed. In (b) the curves for available elastic energy (AEE), available potential energy (APE) and available chemical energy (ACE) are dashed, dashed-dotted and crossed. In both (a) and (b) the curves for the total energy (TE) and kinetic energy (KE) are solid and dotted respectively.

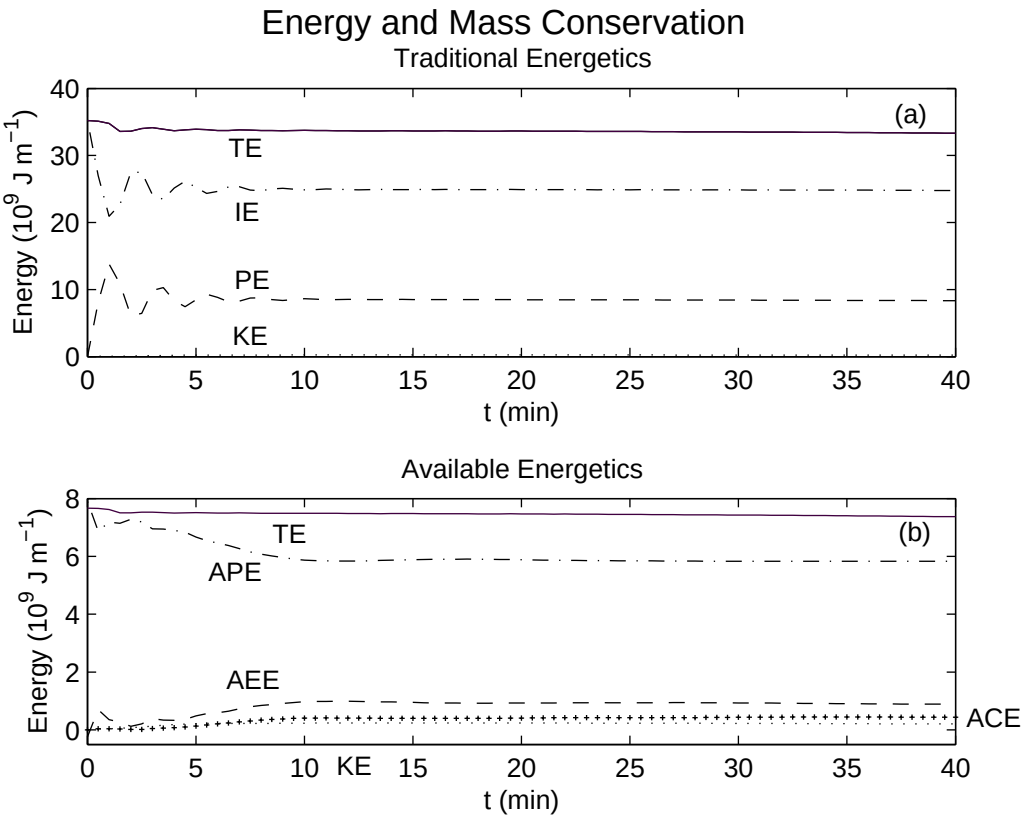

FIG. 11. Domain integrals of the perturbation (a) traditional and (b) available energy in 10^9 J m^{-1} as functions of time for the Satoh thermodynamic scheme. In (a) the curves for internal energy (IE) and potential energy (PE) are dashed-dotted and dashed. In (b) the curves for available elastic energy (AEE), available potential energy (APE) and available chemical energy (ACE) are dashed, dashed-dotted and crossed. In both (a) and (b) the curves for the total energy (TE) and kinetic energy (KE) are solid and dotted respectively.

Chapter 7
Simulation with Full Microphysics

We now consider the traditional and available energetics for a simulation that allows both phase change from water vapor to liquid water, and uses the cloud microphysics scheme detailed in Section 2d to partition the liquid water into cloud water and rainwater.

a. Water budget

The water budget of the atmosphere is shown in Figure 12 and repeated for convenience in Figure 13. These figures show the perturbation of the moisture variables from their initial mass. Except for the water vapor, all the initial masses are zero. Water vapor is cooled and condensed to form cloud water with zero terminal velocity by the updraft formed by the rising warm bubble. Therefore, the water vapor perturbation begins to decrease and the cloud water perturbation increases. Rainwater with a nonzero terminal velocity is then produced by the autoconversion and collection of cloud water, beginning around 14 minutes. Once this rainwater reaches the lower boundary, it is treated as precipitation. The total water represents the sum of the water vapor, cloud water and rainwater perturbations. Through the simulation 7.71×10^4 kg m^{-1} of water is lost from the model domain, but there is 7.83×10^4 kg m^{-1} of precipitation. As the magnitude of the change in the total water is approximately equal to the magnitude of the change in the total precipitation, the mass of water in the model is conserved.

b. Traditional energetics

The traditional energetics for both the Bannon thermodynamic scheme (Fig. 12a) and the Satoh thermodynamic scheme (Fig. 13a) resemble their respective traditional energetics for the case with no phase change (Fig. 10a and 11a) for the first 5 minutes of the simulation. This behavior is expected because the water vapor does not undergo any phase change in this time span. Once the phase change to cloud water occurs, however, the energetics change noticeably.

After the phase change, the internal energy begins to decrease and the potential energy begins to increase in both schemes. As the formulation for the potential and kinetic energy is the same in both schemes, the curves for these quantities in Figures 12a and 13a are identical. The potential energy asymptotes to a constant value of 93.5 x 10^9 J m^{-1}. The kinetic energy increases gradually throughout the simulation to a maximum value of 5.8 x 10^9 J m^{-1}.

As both thermodynamic schemes have different formulations for the enthalpy, they have different formulations of the internal energy and the rain energy. For the Bannon scheme, the rain energy is defined as

$$E_{rain} = \sum m_{rain}(c_{pv}T - l_v), \tag{7.1}$$

and for the Satoh scheme, the rain energy is defined as

$$E_{rain} = \sum m_{rain}c_l T \tag{7.2}$$

where the summation is over all the grid points on the lower boundary of the model domain (see Section 4c). The main difference between the rain energy formulations is that with the Bannon scheme rain energy is defined in reference to the water vapor and hence is negative, but with the Satoh scheme rain energy is defined in reference to the liquid water and hence is positive. The differences in the internal and rain energies only become apparent after 20 minutes when precipitation begins. At this time the previously decreasing internal energy begins to increase under the Bannon thermodynamic scheme (Fig. 12a), yet continues to decrease further under the Satoh thermodynamic scheme (Fig. 13a). Therefore, the total energy of the atmosphere increases with the Bannon scheme to a value of 140 x 10^9 J m^{-1}, and it decreases with the Satoh scheme to a value of -105 x 10^9 J m^{-1}. The rain energy is zero in both schemes until precipitation begins, as it has a dependence on the mass of rainwater that reaches the lower boundary [see both (7.1) and (7.2)]. Once the rainwater does reach the lower boundary, however, the rain energy decreases with time under the Bannon scheme to a value of -148 x 10^9 J m^{-1}, suggesting that the precipitation carries negative energy out of the atmosphere, and leaves behind an atmosphere with relatively increased internal energy. With the Satoh scheme, the rain energy increases with time to a value of 98 x 10^9 J m^{-1} suggesting that the precipitation carries positive energy out

of the atmosphere, and leaves behind an atmosphere with relatively decreased internal energy.

Despite the differences in the internal and rain energies, in both schemes the magnitude of the change in the total energy of the atmosphere, that is, the sum of the internal, kinetic, and potential energies, is approximately equal to the change in magnitude of the rain energy. Therefore, the total energy is approximately conserved.

c. Available energetics

Figures 12b and 13b present the available energetics for the Bannon scheme and the Satoh scheme respectively. Again, in the first 5 minutes of the simulation before the phase change, both scheme's energetics are identical to those presented in Section 6 and Figures 10b and 11b.

After the phase change, however, the energetics for both thermodynamic schemes are very different both from the case of no phase change, and from each other. In the Bannon scheme (Fig. 12b), the phase change from water vapor to cloud water results in a decrease in the available potential energy and an increase in the available elastic energy. As in the case of no phase change, both of these energies mirror each other: as the available potential energy decreases, the available elastic energy increases and vice versa. The available chemical energy can be correlated with the production of rainwater. It begins to increase around 11 minutes when the production of rainwater begins, reaches a maximum when the rainwater peaks around 25 minutes, and then decreases to a final value of -2.1×10^9 J m^{-1} as the mass of rainwater decreases. The total available energy of the atmosphere, which is the sum of the kinetic and available chemical, elastic, and potential energies, is not conserved through the simulation. There is a total decrease of around 20×10^9 J m^{-1} (Table 2).

In the Satoh scheme (Fig. 13b), after the phase change both the available elastic and potential energies have a wave like structure, with the available elastic energy initially increasing slightly, and the available potential energy decreasing. As in the Bannon scheme, both of these energies mirror each other through out the simulation. Overall, both of these energies increase throughout the simulation, following the trend of the total precipitation.

The change in the available chemical energy in this case can be correlated with the change in the total mass of water in the atmosphere, instead of with the mass of rainwater as in the Bannon scheme. The available chemical energy remains approximately zero until around 20 minutes when it begins to decrease. At this time the total mass of water begins to decrease.

Although in this case it appears that the total available energy of the atmosphere is conserved, it is important to note that the *y*-axis of Figure 14b covers a much larger range of values than that of Figure 13b. In fact, the total energy for the Satoh scheme decreases by the same magnitude (20×10^9 J m^{-1}) as the Bannon scheme. Furthermore, the total available energy for both schemes is approximately the same throughout the whole simulation.

To find the reason for the decrease in the total available energy of the atmosphere for both thermodynamic schemes, two further simulations were made. In the first, only the phase change from water vapor to cloud water was allowed; there was no autoconversion from cloud water to rainwater. In the second, all phase changes were allowed, but the rainwater had a zero terminal velocity, that is, there was no fallout of precipitation. Table 2 details the losses in the total available energy of the atmosphere for each simulation.

In the case of only water vapor and cloud water in the model atmosphere, both schemes had a loss of approximately 6×10^9 J m^{-1} of total available energy. Therefore, one third of the 20×10^9 J m^{-1} total energy loss is as a result of the phase change from water vapor to cloud water.

In the case of no fallout, both schemes lost around 10.5×10^9 J m^{-1} of total available energy. Therefore, approximately 4.5×10^9 J m^{-1} is lost in the change of cloud water to rainwater. Consequently, almost half of the total available energy lost is a result of the fallout of rainwater, and the rest is a result of the phase changes.

It is important to note that irrespective of the thermodynamic scheme used, the total available energy losses are the same. Therefore, each thermodynamic scheme only affects the partitioning of the available elastic, potential, and chemical energies, and does not affect the total available energy of the atmosphere.

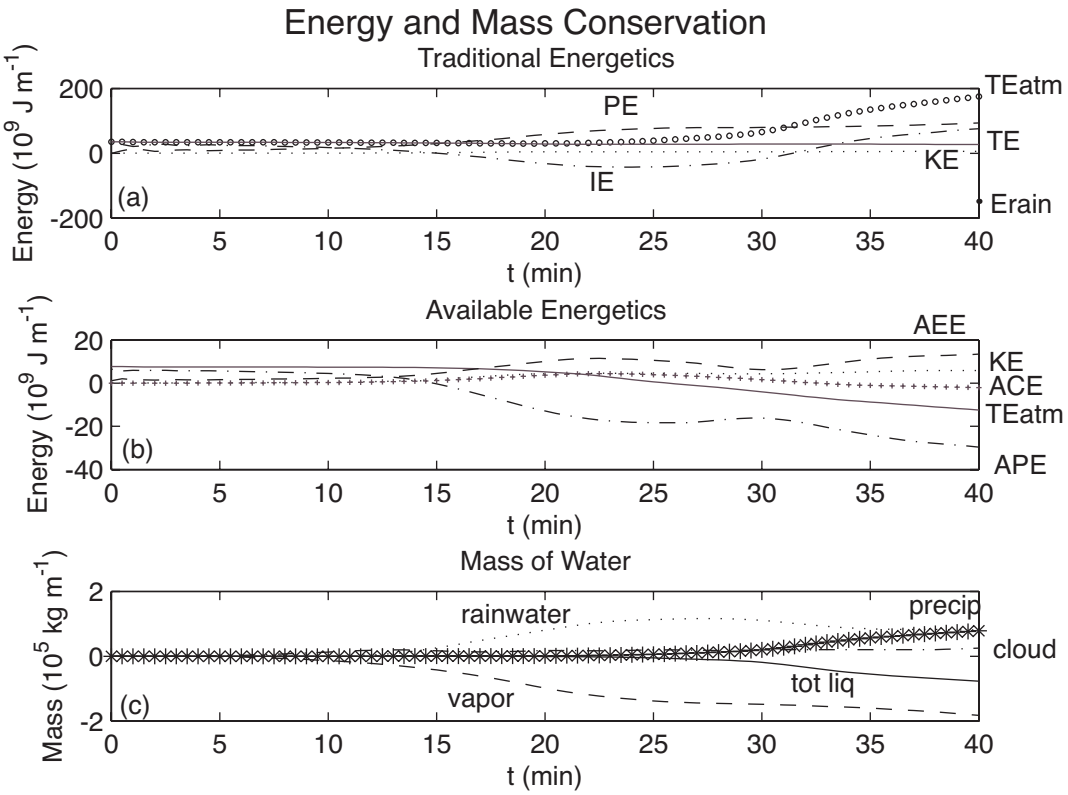

FIG. 12. Domain integrals of the perturbation (a) traditional energetics and (b) available energetics, and (c) moisture variables of the Bannon thermodynamic scheme. In (a) the total energy (solid), IE (dashed-dotted), PE (dashed), TE of the atmosphere (open diamonds), rain energy (closed diamonds), and KE (dotted) are in 10^9 J m^{-1}. In (b) the total available energy (solid) of the atmosphere, ACE (crossed), APE (dashed-dotted), AEE (dashed), and KE (dotted) are in 10^9 J m^{-1}. In (c) the total rainwater (dotted), total vapor (dashed), total cloud water (dashed-dotted), total precipitation (starred), and total liquid (solid) are in 10^5 kg m^{-1}.

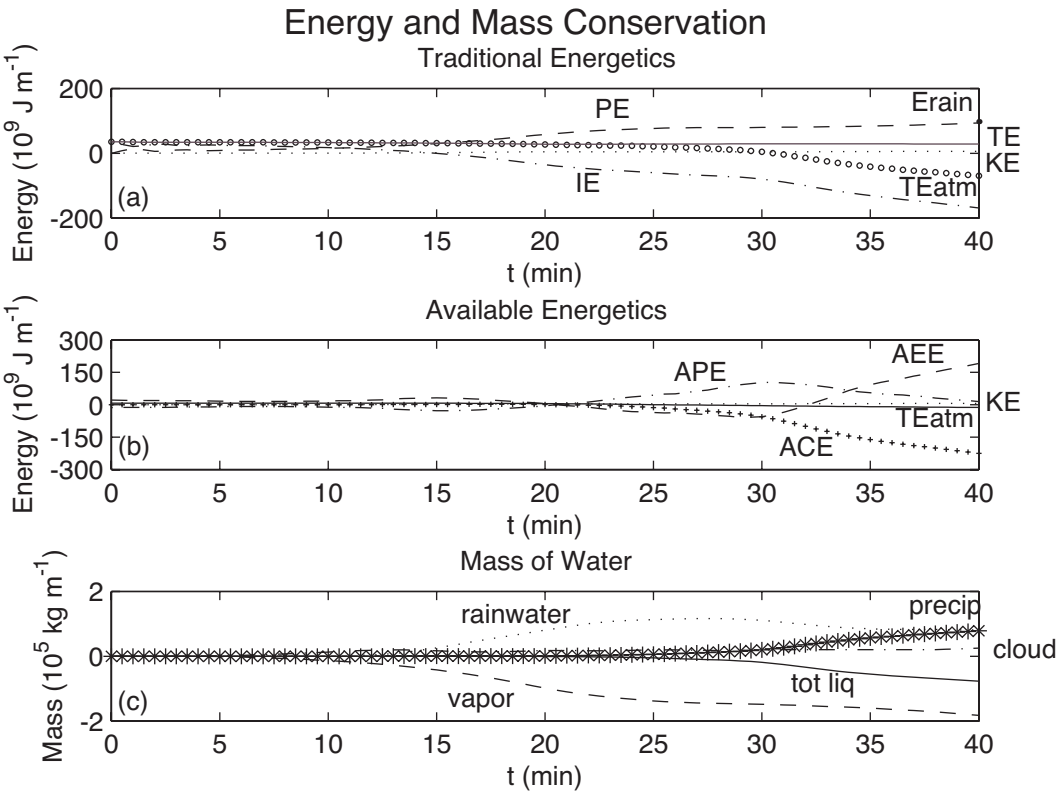

FIG. 13. Domain integrals of the perturbation (a) traditional energetics, (b) available energetics, and (c) moisture variables of the Satoh thermodynamic scheme. In (a) the total energy (solid), IE (dashed-dotted), PE (dashed), TE of the atmosphere (open diamonds), rain energy (closed diamonds), and KE (dotted) are in 10^9 J m^{-1}. In (b) the total available energy (solid) of the atmosphere, ACE (crossed), APE (dashed-dotted), AEE (dashed), and KE (dotted) are in 10^9 J m^{-1}. In (c) the total rainwater (dotted), total vapor (dashed), total cloud water (dashed-dotted), total precipitation (starred), and total liquid (solid) are in 10^5 kg m^{-1}.

TABLE 2. The change in the total available energy of the atmosphere ΔTAEatm of four different simulations for the Bannon thermodynamic scheme with those for the Satoh scheme in parentheses. The total available energy of the initial perturbation is also shown. Positive values indicate an increase in the total energy, negative values indicate a decrease in the total energy, and all values are in units of 10^9 J m^{-1}.

	ΔTAEatm
Initial perturbation	7.66 (7.66)
Simulation with no phase change	-0.29 (-0.29)
Simulation with no rainwater	-5.85 (-6.05)
Simulation with no fallout	-10.51 (-10.71)
Simulation with fallout	-20.14 (-20.34)

Chapter 8
Conclusions

This paper provides a comparison of the energetics of a single-cell thunderstorm in a moist atmosphere generated by an instantaneous diabatic warming using a compressible numerical model. Two different formulations of the moist thermodynamics are presented. Both the traditional and available energetics are compared and contrasted for each of these thermodynamic schemes, and for two separate cases: one with no phase change, and one with full microphysics and fallout.

In the first case with no phase changes, the traditional energetics for both thermodynamic schemes closely resembles the traditional energetics for deep, dry convection given by Smith and Bannon (2008). Initially the internal energy perturbation contains all of the energy perturbation from the diabatic warming. As the warm bubble rises, the mass aloft increases, hence increasing the potential energy, and decreasing the internal energy through adiabatic cooling. The internal and potential energies both demonstrate oscillatory behavior because of long wavelength vertically propagating acoustic modes. A small amount of kinetic energy exists in the model domain.

The available energetics of both thermodynamic schemes also closely resemble the available energetics of Smith and Bannon (2008), with the addition of the available chemical energy. Under the Bannon (2005) scheme, the energy of the diabatic warming is contained in the available potential and elastic energies. These energies exhibit a damped oscillation similar to that in the traditional energetics. Under the Satoh (2003) scheme, the energy of the diabatic warming creates a positive perturbation in the available potential energy and a negative perturbation in the available elastic energy. Again these energies exhibit a damped oscillation similar to that in the traditional energetics, but the initial amplitude is slightly greater than that under the Bannon scheme. The available chemical energy increases and the available potential energy decreases by the same amount under both thermodynamic schemes. The decrease in the total energy is the same with both schemes.

In the second case the full cloud microphysics scheme of Kessler (1969) is used. Here water vapor cools and condenses to form cloud water with zero terminal velocity. Autoconversion and collection of the cloud water then forms rainwater with a nonzero terminal velocity. This rainwater is allowed to fall to the lower boundary and leave the model domain, resulting in a net loss of water from the atmosphere.

For the traditional energetics both thermodynamic schemes conserve total energy, although each scheme does so in a different way. As the potential and kinetic energies do not depend on the formulation of the thermodynamics, these are the same for each scheme. The internal and rain energy formulations, however, differ for each scheme. In both schemes, the internal energy begins to decrease once the phase change from water vapor to cloud water begins, however with the onset of precipitation, under the Bannon scheme the internal energy begins to increase, whereas under the Satoh scheme it continues to decrease. Furthermore, under the Bannon scheme the rain energy is a negative quantity, but under the Satoh scheme it is a positive quantity. Considering both of these differences suggests that, when using the Bannon thermodynamic scheme, the precipitation carries negative energy out of the model domain and leaves behind an atmosphere with increased internal energy. When using the Satoh scheme, however, the precipitation carries positive energy out of the model domain and leaves behind an atmosphere with decreased internal energy.

For the available energetics, both thermodynamic schemes formulate each energy differently. As in the case with no phase change, the available internal and potential energies in both schemes mirror each other. Overall, however, in the Bannon scheme, the available elastic energy increases, and the available potential energy decreases throughout the simulation, whereas in the Satoh scheme, both the available elastic and available potential energies increase throughout the simulation. In the Bannon scheme there appears to be a correlation between the available chemical energy and the mass of rainwater in the atmosphere, but in the Satoh scheme there appears to be a correlation between the available chemical energy and the total mass of water in the atmosphere.

With both thermodynamic schemes there is a total available energy loss of approximately 20×10^9 J m^{-1} from the model atmosphere. By considering two further

model simulations not presented in this paper, it was found that for each thermodynamic scheme approximately half of the total available energy loss is a result of the phase changes from water vapor to cloud water, and from cloud water to rainwater. The other half is as a result of the loss of water because of precipitation fallout.

This study has shown that both thermodynamic schemes provide different interpretations of the internal, rain, available chemical, available elastic, and available potential energies. In regards to the traditional energetics, the two formulations of the enthalpy lead to differing conclusions to the role of precipitation in the energetics of a single-cell thunderstorm. With the available energetics, however, the change in the total available energy over the forty minute simulation is the same, irrespective of the thermodynamic scheme used. Further work is required to formulate both the available phase change and available rain energies for both thermodynamic schemes. In addition, this work should also be extended to a more realistic cloud microphysics parameterization that includes ice processes.

REFERENCES

Bannon, P. R., 2005: Eulerian available energetics in moist atmospheres. *J. Atmos. Sci.,* **62,** 4238-4252.

Bohren, C. F., and B. A. Albrecht, 1998: *Atmospheric Thermodynamics*. Oxford University Press, 402pp..

Bryan, G. H., and J. M. Fritsch, 2002: A benchmark simulation for moist nonhydrostatic numerical models. *Mon. Wea. Rev.,* **130,** 2917-2928.

Bryan, G. H., J. C. Wyngaard, and J. M. Fritsch, 2003: Resolution requirements for the simulation of deep moist convection. *Mon. Wea. Rev.*, **131,** 2394-2416.

Byers, H. R., and R. R. Braham Jr., 1948: Thunderstorm structure and circulation. *J. Meteor.,* **5,** 71-86.

Doswell, Charles, A., III, and P. M. Markowski, 2004: Is buoyancy a relative quantity? *Mon. Wea. Rev.,* **132,** 853-863.

Durran, D. R., and J. B. Klemp, 1983: A compressible model for the simulation of moist mountain waves. *Mon. Wea. Rev.,* **111,** 2341-2361.

Emanuel, K. A., 1994: *Atmospheric Convection.* Oxford University Press, 580pp..

Fanelli, P. F., and P. R. Bannon, 2005: Nonlinear atmospheric adjustment to thermal forcing. *J. Atmos. Sci.,* **62,** 4253-4272.

Hausman, S.A., K.V. Ooyama, and W.H. Schubert, 2006: Potential vorticity structure of simulated hurricanes. *J. Atmos. Sci.*, **63,** 87-108.

Holton J.R., 2004: *An Introduction to Dynamic Meteorology,* 4th ed, Elsevier, 535pp..

Kessler, E., 1969: *On the distribution and continuity of water substance in atmospheric circulation*. *Meteor. Monogr.,* No. 32, Amer. Meteor. Soc., 84 pp..

Lorenz, E. N., 1955: Available potential energy and the maintenance of the general circulation. *Tellus,* **7,** 157-167.

Margules, M., 1905: On the energy of storms. *Smithson. Misc. Collect.,* **51,** 535-595. (Translated by C. Abbe.)

Moncrieff, M. W., and M. J. Miller, 1976: The dynamics and simulation of tropical squall lines. *Quart. J. Roy. Meteor. Soc.,* **102,** 373-394.

Satoh, M., 2003: Conservative scheme for a compressible nonhydrostatic model with moist processes. *Mon. Wea. Rev.,* **131,** 1033-1050.

Smith, J. W., and P. R. Bannon, 2008: A comparison of compressible and anelastic models of deep dry convection. *Mon. Wea. Rev.,* (in press).

Wang, J., and D. A. Randall, 1996: A cumulus parameterization based on the generalized convective available potential energy. *J. Atmos. Sci.,* **53,** 716-727.

Weisman, M. L., and J. B. Klemp, 1982: The dependence of numerically simulated convective storms on vertical wind shear and buoyancy. *Mon. Wea. Rev.,* **110,** 504-520.

Weisman, M. L., and J. B. Klemp, 1984: The structure and classification of numerically simulated convective storms in directionally varying wind shears. *Mon. Wea. Rev.,* **112,** 2479-2498.

Williams, E., and N. Renno, 1993: An analysis of the conditional instability of the tropical atmosphere. *Mon. Wea. Rev.,* **121,** 21-36.